Nile Red fluorescence spectroscopy reports early physicochemical changes in myelin with high sensitivity

Wulin Teo[a,1], Andrew V. Caprariello[a,1], Megan L. Morgan[a], Antonio Luchicchi[b], Geert J. Schenk[b], Jeffrey T. Joseph[a,c], Jeroen J. G. Geurts[b], and Peter K. Stys[a,2]

[a]Department of Clinical Neurosciences, Hotchkiss Brain Institute, University of Calgary Cumming School of Medicine, Calgary, AB T2N 4N1, Canada; [b]Department of Anatomy and Neurosciences, Amsterdam UMC, Vrije Universiteit, Amsterdam Neuroscience, 1081 HZ Amsterdam, The Netherlands; and [c]Department of Pathology and Laboratory Medicine, University of Calgary, Calgary, AB T2N 4N1, Canada

The molecular composition of myelin membranes determines their structure and function. Even minute changes to the biochemical balance can have profound consequences for axonal conduction and the synchronicity of neural networks. Hypothesizing that the earliest indication of myelin injury involves changes in the composition and/or polarity of its constituent lipids, we developed a sensitive spectroscopic technique for defining the chemical polarity of myelin lipids in fixed frozen tissue sections from rodent and human. The method uses a simple staining procedure involving the lipophilic dye Nile Red, whose fluorescence spectrum varies according to the chemical polarity of the microenvironment into which the dye embeds. Nile Red spectroscopy identified histologically intact yet biochemically altered myelin in prelesioned tissues, including mouse white matter following subdemyelinating cuprizone intoxication, as well as normal-appearing white matter in multiple sclerosis brain. Nile Red spectroscopy offers a relatively simple yet highly sensitive technique for detecting subtle myelin changes.

lipids | fluorescence spectroscopy | spectral confocal microscopy | multiple sclerosis | cuprizone

Myelin is a highly ordered, lipid-rich extension of glial cell membrane that facilitates rapid and efficient saltatory conduction of action potentials along axons in the central and peripheral nervous systems. The stability of myelin membranes critically depends on its molecular composition (1–3). Although myelin is maintained roughly at a ratio of 70:30% lipid to protein (4), lipid membranes are highly fluid; changes in lipid composition are defining characteristics of myelin development (5), homeostasis in the adult, and aging in rodents (6, 7), as well as primates (8). Shifts in lipid composition also occur in inflammatory demyelinating disorders like multiple sclerosis (MS) (9, 10). Lipids are even theorized to be targets of immune attacks in autoimmune disorders, a role previously ascribed to proteins (11). Key roles for lipids notwithstanding, tools to interrogate biochemical changes to myelin lipids have largely been restricted to in vitro systems.

Once thought to be inert, myelin is now known to be a chemically and structurally dynamic element (12). Specific combinations of proteins and lipids induce formation and compaction of multilamellar vesicles that resemble myelin (13), underscoring the importance of correct chemical composition for assembly. Conversely, alterations in these molecular proportions promote decompaction and myelin vesiculation (3, 14). The polarity of lipid species in cell membranes influences their packing properties and therefore stability (15). Governed by competing thermodynamic forces of lipid curling and hydrocarbon packing (16), myelin sheaths lie at the critical edge of bilayer stability and thus are susceptible to factors in the environment. Indeed, the myelin integrity theory of MS rests on the outsized influence of environmental forces on myelin stability and function (17). Therefore, methods for detecting physicochemical changes in myelin lipid composition in situ would greatly enhance our understanding of early events in myelin development, as well as myelin damage in disease states, with important implications for therapies designed to prevent myelin loss in MS and other demyelinating disorders.

The study of myelin lipid biochemistry poses unique challenges (18). Traditional analytical methods, such as thin-layer chromatography and high-performance liquid chromatography (19), depend on tissue homogenization that eliminates informative spatial relationships. Imaging lipid mass spectrometry (20) preserves spatial relationships, but submicron resolution has yet to be realized, and reproducibility at the level of sample preparation remains problematic (21). Coherent anti–Stokes Raman scattering microscopy provides high-resolution, label-free imaging of lipids in histological samples (22), but this method lacks sensitivity and requires expertise in nonlinear optics as well as highly specialized hardware. Finally, fluorescent lipophilic dyes, though widely available and easy to use, have traditionally been employed to detect lipid-rich structures in only a qualitative manner. Conventional fluorescence microscopy is therefore unable to detect subtle shifts in lipid biochemistry. By contrast, Nile Red (NR) is a fluorescent dye that is well situated to report changes in the chemical polarity of cell membranes and myelin, being both lipophilic (23, 24) and differentially fluorescent depending on solvent environment (i.e., exhibits solvatochromism) (25). The current study uses NR fluorescence spectroscopy to identify polarity shifts as an early manifestation of myelin disease prior to overt demyelination. We

Significance

Many diseases of the nervous system affect white matter and myelin, the critical lipid-rich insulating material enveloping axons. We report a method based on solvatochromic fluorescent probes and spectral microscopy that detects very early pathological changes in myelin in both a rodent model and in postmortem human multiple sclerosis brain at a stage that precedes overt histological myelin loss. Our method reveals that multiple sclerosis white matter exhibits widespread changes in myelin dielectric constant in areas distant from typical inflammatory demyelinating lesions. Fluorescence spectroscopy using solvatochromic lipid probes such as Nile Red has the ability to report, with high sensitivity and in a quantitative manner, early physicochemical changes in cells and tissues that precede pathological alterations detectable by conventional histological methods.

NEUROSCIENCE

show that this technique reports subtle biochemical changes in myelin, resulting in a method that is a very sensitive marker of incipient myelin injury.

Results

Nile Red Fluorescence Reports Chemical Polarity of the Local Environment. Fig. 1*A* illustrates how chemical polarity changes NR fluorescence. The dye was dissolved in solvents of various known polarities at a concentration of 20 μM and excited by 370 nm light. In nonpolar solvents like hexane, the dye emitted at a shorter wavelength (green), whereas in a relatively polar solvent such as methanol, fluorescence was red-shifted. Corresponding emission spectra (Fig. 1*B*) underscore the substantial ∼100-nm shift due to the solvatochromic properties of NR. Unnormalized spectra (Fig. 1*C*) demonstrate differential quantum yield of the dye depending on solvent polarity; fluorescence intensity was 50-fold greater in nonpolar hexane compared to highly polar solvents such as water.

We next sought to test whether isolated lipids of varying polarities also elicited differential NR fluorescence. As with nonpolar solvents (Fig. 1 *A–C*), nonpolar cholesterol (violet, 0.25 M in a solution of NR and phosphate-buffered saline [PBS]) yielded more blue-shifted fluorescence compared to phospholipids (red, 0.02 M), whose polar phosphate and choline head groups elicited red-shifted fluorescence (Fig. 1*D*). Isolated sulfatide (green, 0.1 M), with its intermediately polar sulfate head group, elicited a NR emission peak between that of cholesterol and phospholipid. To confirm that such differences would also apply in a more biologically relevant model, we stained cultured

MO3.13 cells after paraformaldehyde fixation with 14 μM NR (*SI Appendix*, Fig. S1). Delipidation with chloroform:methanol decreased NR fluorescence by ∼10-fold, indicating that the vast majority of NR signal originated from labile cellular lipids. Selective depletion of cholesterol, a prevalent nonpolar lipid in cells (*SI Appendix*, Fig. S2), increased mean polarity reported by NR fluorescence as expected. Finally, treating 1,2-dioleoyl-sn-glycero-3-phosphocholine (DOPC)-containing giant unilamellar vesicles with phospholipase A2, an enzyme that cleaves polar glycerophosphocholine heads from DOPC, releasing these polar moieties from the membrane (26), thereby enriching the vesicles in the remaining less polar acyl chains, induced an expected spectral blue-shift and drop in measured polarity (*SI Appendix*, Fig. S2 *B and C*). Collectively, these data show that solutions of pure solvents, lipids, or cellular fluorescence elicit reproducible, polarity-dependent NR emissions. We therefore chose to use solvent spectra as references against which one can assign relative polarities to myelin lipids in tissue.

Nile Red as an Indicator of Lipid Polarity in Tissue. We next asked whether solvent reference spectra generated in Fig. 1 could be used in postprocessed images to detect differences in tissue "micropolarity" between different regions of adult mouse brain. To these ends, tissue staining methods were developed that would simultaneously resolve fine histological features and report lipid polarity differences between brain structures. Fig. 2*A* shows spectral confocal micrographs of fixed, healthy mouse brain cryosections incubated for 10 min in 10 μM NR solution. The true-color image
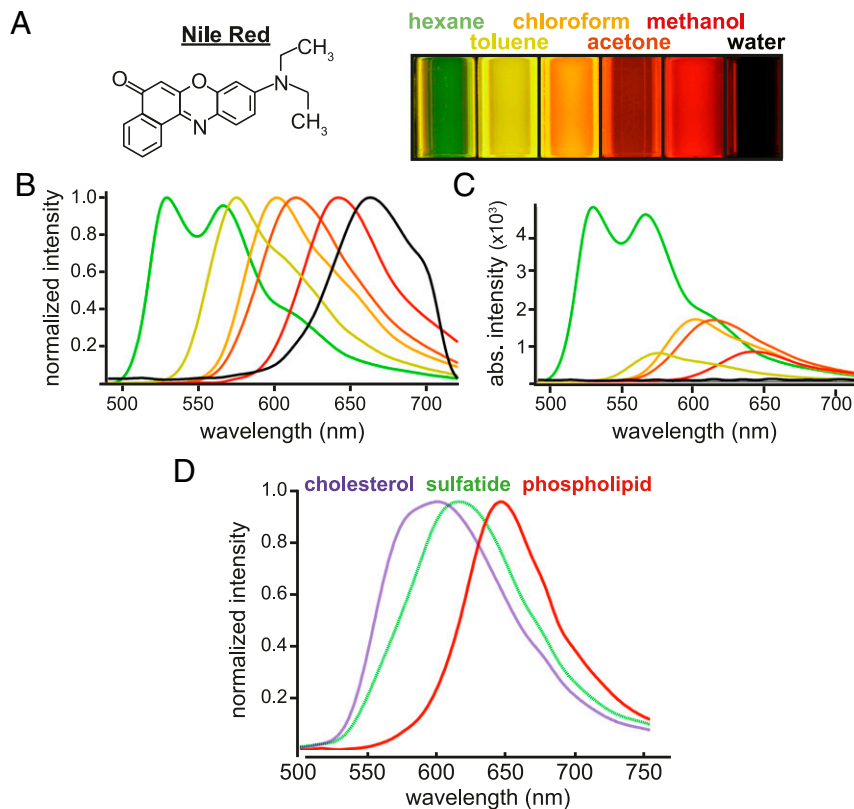
Fig. 1. NR fluorescence varies with polarity of its environment. (*A*) Cuvettes of NR (10 μM) dissolved in solvents of varying polarity (nonpolar hexane to highly polar water) and excited with 380 nm light demonstrate a substantial color shift of emitted fluorescence; more polar solvents resulted in less intense and longer-wavelength emission. (*B*) Normalized fluorescence emission spectra from the six solvents. (*C*) Unnormalized emission spectra underscore the inverse relationship between NR signal intensity and solvent polarity. (*D*) As with different solvents in *A*, less-polar lipids (cholesterol) elicited blue-shifted NR fluorescence, which progressed to longer wavelengths as the polarity of the lipid increased. This strong solvatochromic property of NR formed the basis of the spectroscopic tissue imaging method described in this study.

(calculated to approximate what the human eye would see when viewing under a conventional fluorescence microscope) showed a brightly stained section with definition of major brain regions, in particular lipid-rich white matter tracts such as corpus callosum and anterior commissure. However, the perceived color was uniformly orange, with contrast generated mainly by intensity differences proportional to lipid content, as would be expected for a lipophilic dye. By contrast, a postprocessed image in which each pixel was pseudocolored according to its spectral shape relative to a pair of solvent references revealed both morphological and chemical details (Fig. 2 A, Lower). For example, in addition to enhancing the contrast between gray and white matter (e.g., cortex versus corpus callosum, respectively), the green hues of the corpus callosum and anterior commissure reflect the higher content of less-polar lipids compared to gray matter structures, in which a redder hue indicates a greater proportion of more polar species. A
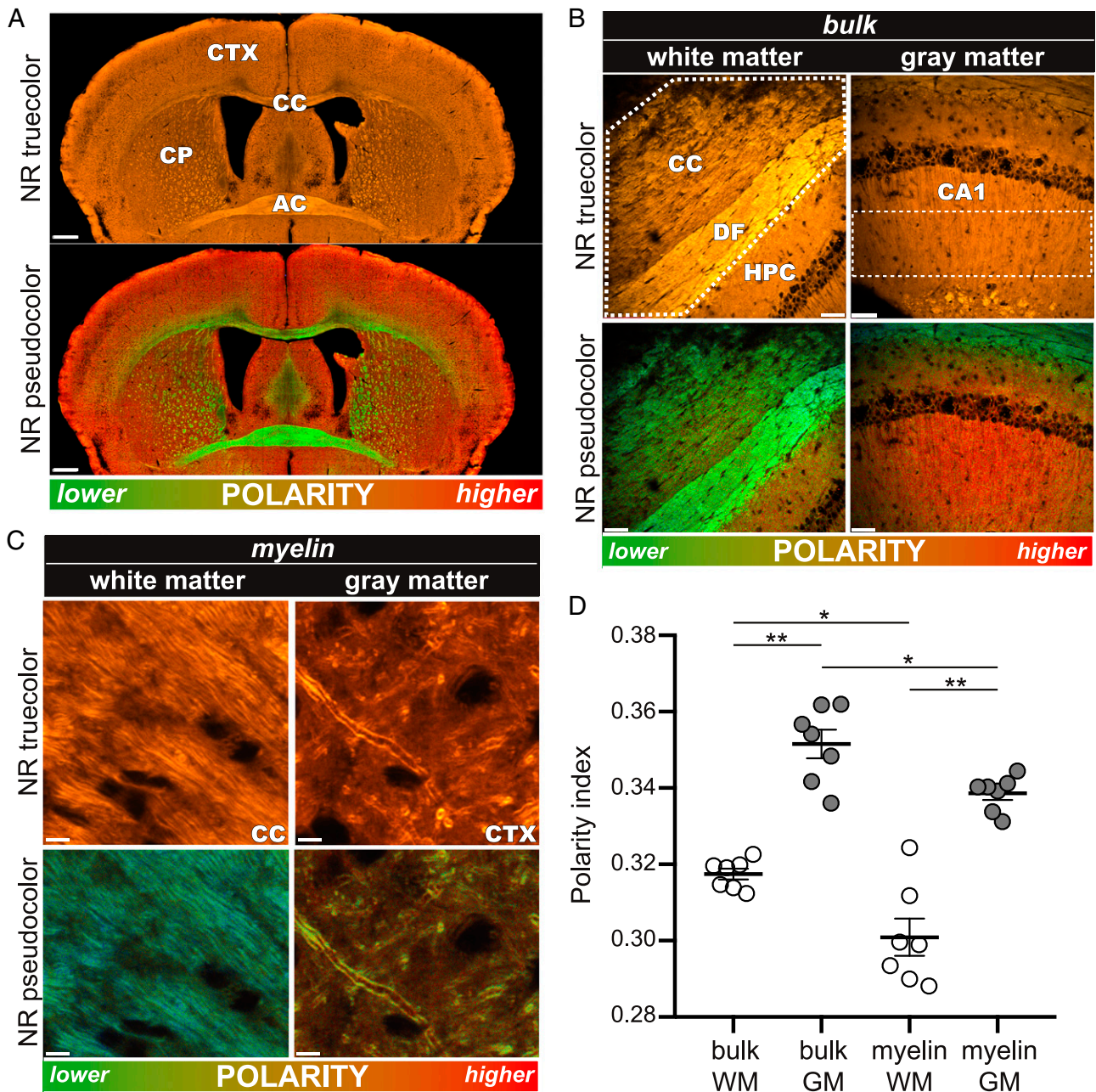
Fig. 2. NR fluorescence spectroscopy illuminates the physicochemical state of healthy rodent myelin in white versus gray matter. (A, Top) A true-color image of a healthy mouse brain stained with NR. Contrast is generated by lipophilic NR, preferentially binding to the brain's lipid-rich compartments, especially myelin-rich corpus callosum (CC) and anterior commissure (AC). (A, Bottom) The pseudocolor image designed to map tissue polarity to a different display color more clearly reveals substantial contrast between gray and white matter regions. (B) Higher-magnification true-color (Top) and pseudocolor (Bottom) images illustrate marked polarity differences in CC and adjacent hippocampus in healthy rodent. (C) NR labeling provides excellent spatial resolution so that individual myelin sheaths can be resolved. (D) The graph depicts the mean polarity index derived from NR spectra in various regions. White matter exhibited a consistently lower polarity than gray matter. Each marker represents the average value of multiple images of the same subject. The significance was determined by one-way ANOVA. CP, caudate putamen; CTX, cortex; DF, dorsal fornix; HPC, hippocampus; CA1, stratum radiatum region of the hippocampus. (Scale bars: A, 500 μm; B, 50 μm; and C, 5 μm.) *$P < 0.05$; **$P < 0.01$.

Teo et al.
Nile Red fluorescence spectroscopy reports early physicochemical changes in myelin with high sensitivity

PNAS | 3 of 11
https://doi.org/10.1073/pnas.2016897118

whole-brain map of relative chemical polarities can thereby be rendered.

We then performed a higher-resolution analysis of selected gray and white matter structures to test for biochemical heterogeneity in healthy tissue and in myelin in particular. Fig. 2*B* shows a "bulk" analysis (i.e., all cellular elements combined, shown by the dashed outline) of white versus gray matter from corpus callosum/hippocampus. While the true-color images showed good morphological definition, the pseudocolored equivalents (*Materials and Methods*) additionally revealed substantial differences in lipid polarity between white and gray matter, similar to the overview image in Fig. 2*A*. Differences between the polarities of white versus gray matter—the latter known to include a greater proportion of protein and water-rich cytosolic regions—validated our pseudocoloring algorithm and prompted us to examine myelin in white versus gray matter in more detail. Fig. 2*C* shows higher magnification micrographs in which individual myelinated axons were resolved. In contrast to bulk tissue analysis, here we selected only the myelin sheaths for spectral analysis. Interestingly, white matter myelin exhibited a lower polarity than that found in gray matter, though myelin in both regions was less polar than the surrounding parenchyma, data that are quantitatively summarized in Fig. 2*D*.

Biochemically Altered Myelin in Predemyelinated Tissue. To identify whether subtle changes in myelin lipids precede imminent demyelination, we turned to an established model of delayed demyelination using oral intoxication with the copper-chelator cuprizone (CPZ) (27). Fixed, frozen tissue sections from mice treated with CPZ (0.2% weight/weight [wt/wt]) for 2, 7, and 14 d (exposure periods too brief to induce histological demyelination; Fig. 3 *A* and *B*) were stained with NR (Fig. 2) so that subtle shifts in polarity during the early, predemyelinating phase of CPZ could be studied. After only 2 d of CPZ, we observed an increase in the mean polarity of lipids in the medial corpus callosum—a brain region with known susceptibility to CPZ-induced demyelination—compared to untreated control brains (Fig. 3*C*). Consistent with the selective loss of nonpolar lipids, significant accumulation of nonpolar (i.e., blue-shifted) lipid droplets was observed adjacent to the ventricles (*SI Appendix*, Fig. S3). Interestingly, these only became enriched in cholesterol at later time points (28 d of CPZ exposure), consistent with previous reports of cholesterol release once myelin begins to degenerate (28). The mean polarity of the corpus callosum remained significantly increased throughout the 2-wk sub-demyelinating CPZ exposure compared to naïve controls (Fig. 3*D*), indicative of persistent biochemical abnormalities in the absence of histological myelin loss.

Altered Myelin Biochemistry Identifies MS Lesion "Hotspots." We next asked whether polarity changes may be an early event in human MS brain, hypothesizing that histologically intact but biochemically altered myelin represents "hotspots" of susceptibility to demyelination. Autopsied MS brain tissue from normal-appearing white matter (NAWM) was stained with NR and spectrally imaged as in Figs. 2 and 3. Pseudocolored images of periventricular white matter from non–MS controls were spectrally homogeneous (violet, Fig. 4*A*). In striking contrast, the MS white matter adjacent to the ventricular surface exhibited heterogeneous spectral character, with periventricular regions in particular shifting to higher polarity (Fig. 4*B*). A red-to-violet gradient (Fig. 4*D*) from the ventricle into the tissue parenchyma—which CPZ data would suggest represents a gradient of pathology from the ventricular surface extending into the brain—was paralleled by the density of spheroids (white arrows, Fig. 4*D*; *SI Appendix*, Fig. S4). NR spectroscopy also illuminated focal regions of white matter susceptibility in areas remote from overt periventricular lesions. For example, the dotted rectangle in Fig. 4*E* demonstrates a common observed focal region of

red-shifted NR emissions in the absence of frank demyelination [orange NR + green myelin basic protein (MBP), Fig. 4*F*].

Diffuse Myelin Injury in MS Normal-Appearing White Matter. To broadly assess the extent to which NR abnormalities in MS tissue represent diffuse rather than focal events, we analyzed NR fluorescence in large areas of normal-appearing white and gray matter from MS specimens. Low-magnification true-color images were unrevealing with respect to morphology or perceptible color differences (Fig. 5*A*, top two true-color panels). In contrast, spectral pseudocoloring (Fig. 5*A*, bottom two panels) showed widespread changes in NR emission in the bulk white matter consistent with significant shifts toward higher chemical polarity, similar to what was observed in both predemyelinated CPZ mouse white matter as well as periventricular MS tissues (Figs. 3 and 4, respectively). Gray matter in MS tissue was also affected; however, analysis of all pixels in a given image ("bulk gray matter," Fig. 5*B*) indicated a change in the opposite direction, toward a more blue-shifted, less polar character.

Next, we analyzed individual myelinated axons in both the white and gray matter. Strikingly, whereas myelin sheaths in healthy control white matter sections were uniformly nonpolar with a tight distribution, MS myelin was much more heterogeneous with a shift to more polar character (Fig. 5*C*, white arrows), despite the fact that the myelin appeared structurally normal (Fig. 5*C*, top two panels). We also observed numerous swollen axons, typical of nondemyelinated MS white matter (29), that exhibited a bright, red-shifted fluorescence. These results indicate that there are widespread polarity changes in MS that extend well beyond histologically demyelinated areas, with the myelin compartment being particularly affected. Taken together, our data indicate that biochemical injury to myelin is a widespread phenomenon in the MS brain and may be a key early pathological feature.

Discussion

Tools to monitor subtle changes in the chemistry of tissue lipids are limited, particularly when preservation of tissue architecture is required and high-resolution images of cellular details are desired. NR is a lipophilic dye well known for its ability to label cell membranes and other lipid-rich tissue components (30, 31), including lipid droplets (32), and has also been used to label living organisms (33). The dye belongs to a class of fluorescent molecules whose emission spectrum varies according to the polarity of its microenvironment, a property known as solvatochromism (34). NR fluorescence becomes less intense and shifts to longer wavelengths in more polar environments; intramolecular charge transfer during the $S_0 \rightarrow S_1$ transition induces a large change in the molecule's dipole moment, increasing its interactions with polar solvents and thereby shifting its emission to longer wavelengths (35, 36) (Fig. 1). This probe also interacts strongly with anisotropic media such as nematic liquid crystals, which exert effects on its absorption and fluorescence spectra (35). Given the lipid-rich character and liquid crystalline properties of myelin (37), we reasoned that a lipophilic solvatochromic probe such as NR would be a useful reporter of physicochemical properties of myelin sheaths while at the same time serving as a bright label to provide high-resolution morphological detail. In line with our expectation, this dye produced bright staining of both gray and white matter regions of paraformaldehyde-fixed cryosections of mouse brain (Fig. 2). We chose this processing method rather than paraffin embedding which requires organic solvents for dewaxing that would partially delipidate the samples and potentially distort the NR signals.

In tissue sections of naive mouse brains, NR labeling revealed detailed cellular morphology in both gray and white matter regions (e.g., Fig. 2). Contrast was exclusively provided by intensity variations, particularly apparent between gray matter and lipid-rich white matter areas; no differences in hue were perceptible
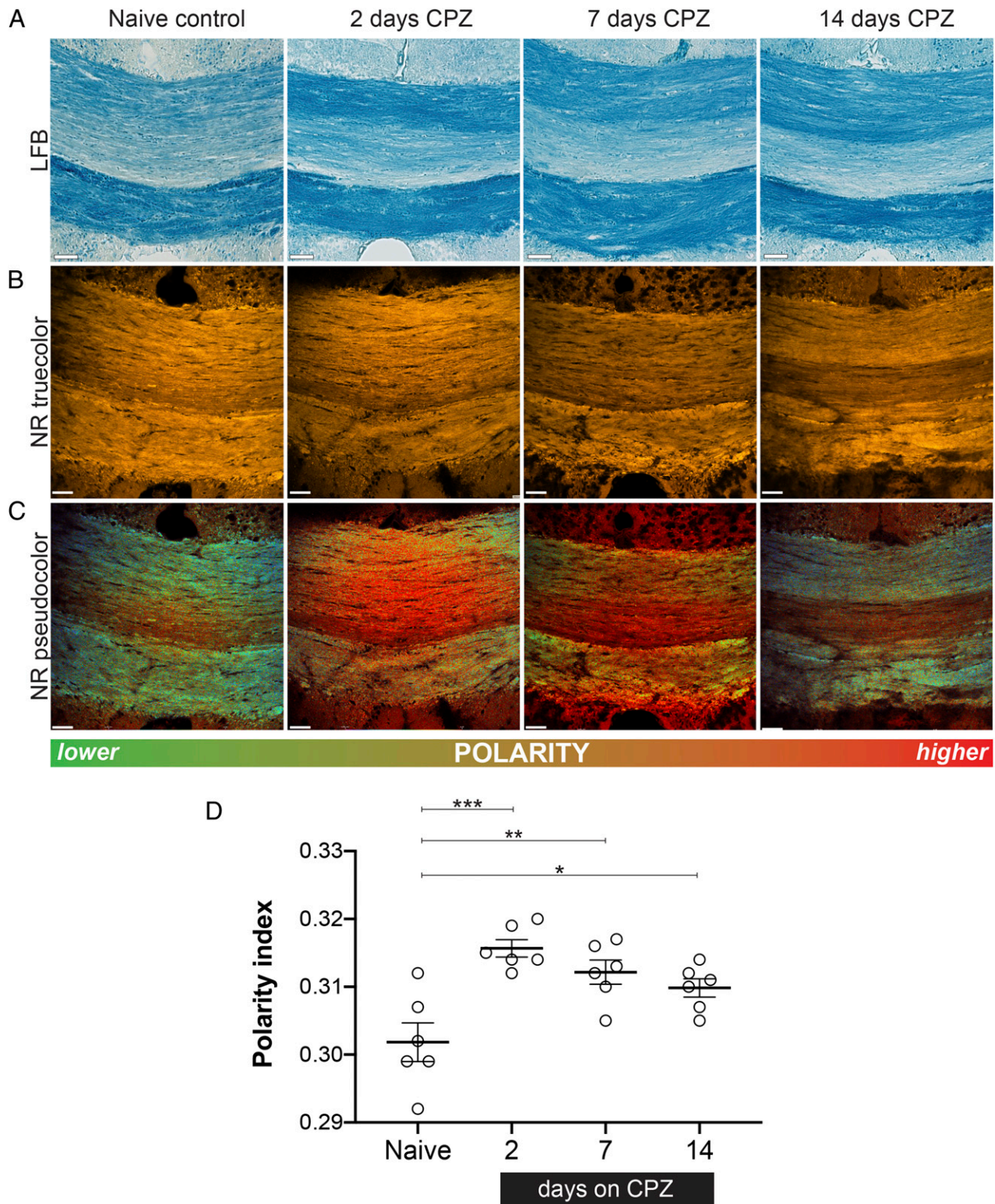
Fig. 3. Early myelin changes revealed by NR spectroscopy precede overt demyelination in the CPZ mouse model. (*A*) LFB staining indicates that no histologically detectable demyelination occurred during the 2-wk treatment with CPZ using this conventional myelin label. (*B*) True-color images of NR-labeled medial CC from control and after various exposure times to CPZ. By signal intensity alone, there is no detectable myelin loss after 14 d of intoxication. (*C*) Equivalent pseudocolor images reveal a significant polarity shift to higher values as early as 2 d of CPZ exposure, with partial recovery at later time points. (*D*) Quantitative depiction of mean polarity index as a function of CPZ exposure. The partial reversal toward normal at later times likely reflects the robust reparative mechanisms in the rodent. The significance was determined by one-way ANOVA, followed by a post hoc Dunnett test. (Scale bar, 50 μm.) *$P < 0.05$; **$P < 0.01$; and ***$P < 0.001$.
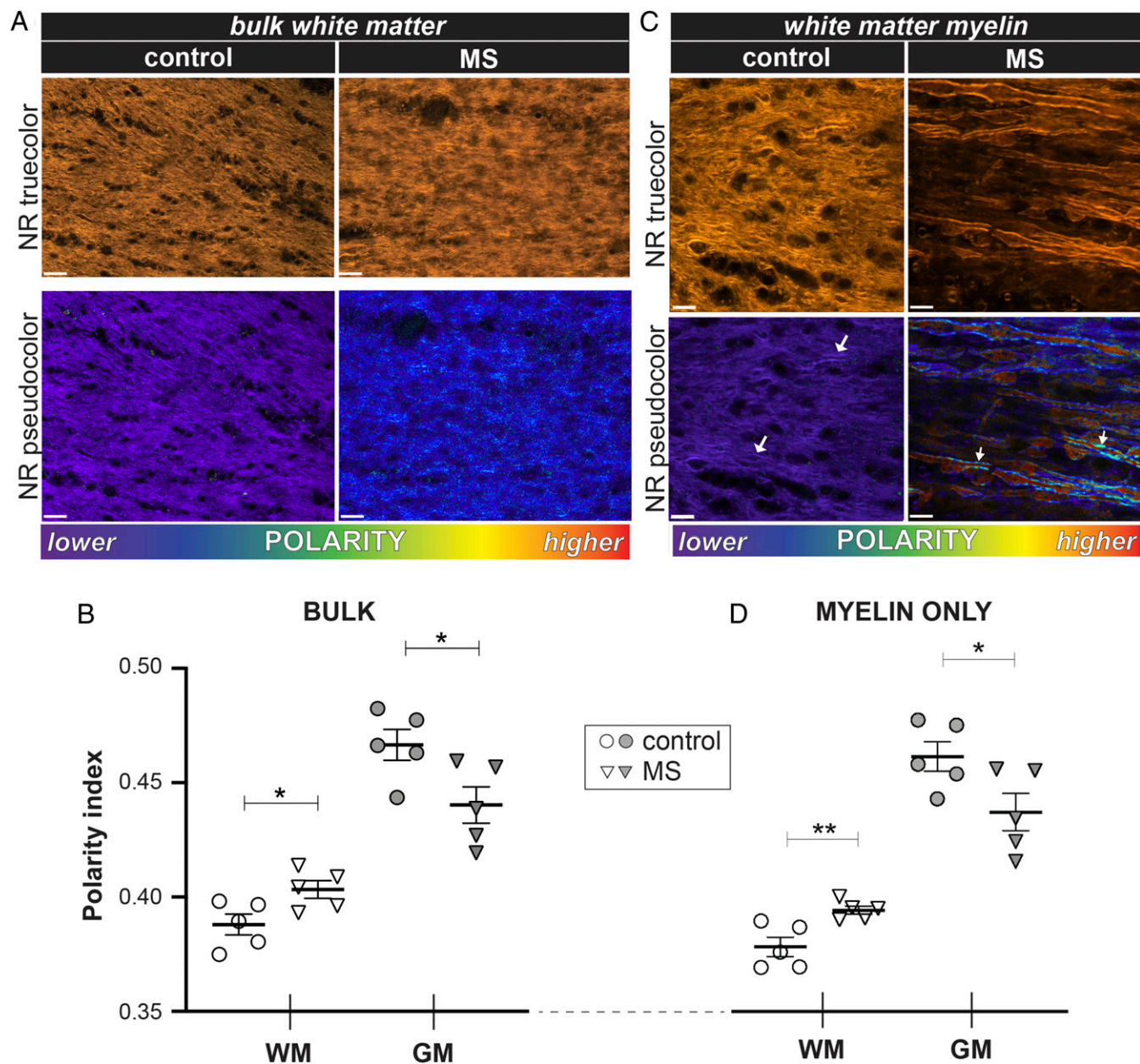
by the naked eye. However, spectroscopy revealed significant differences in the chemical polarities of bulk gray versus white matter, with the former exhibiting a more polar character (Fig. 2D) owing to a higher lipid content. Notably, such differences would not be detected by standard epifluorescence microscopy. Unexpectedly, our method also revealed significant differences in chemical polarity
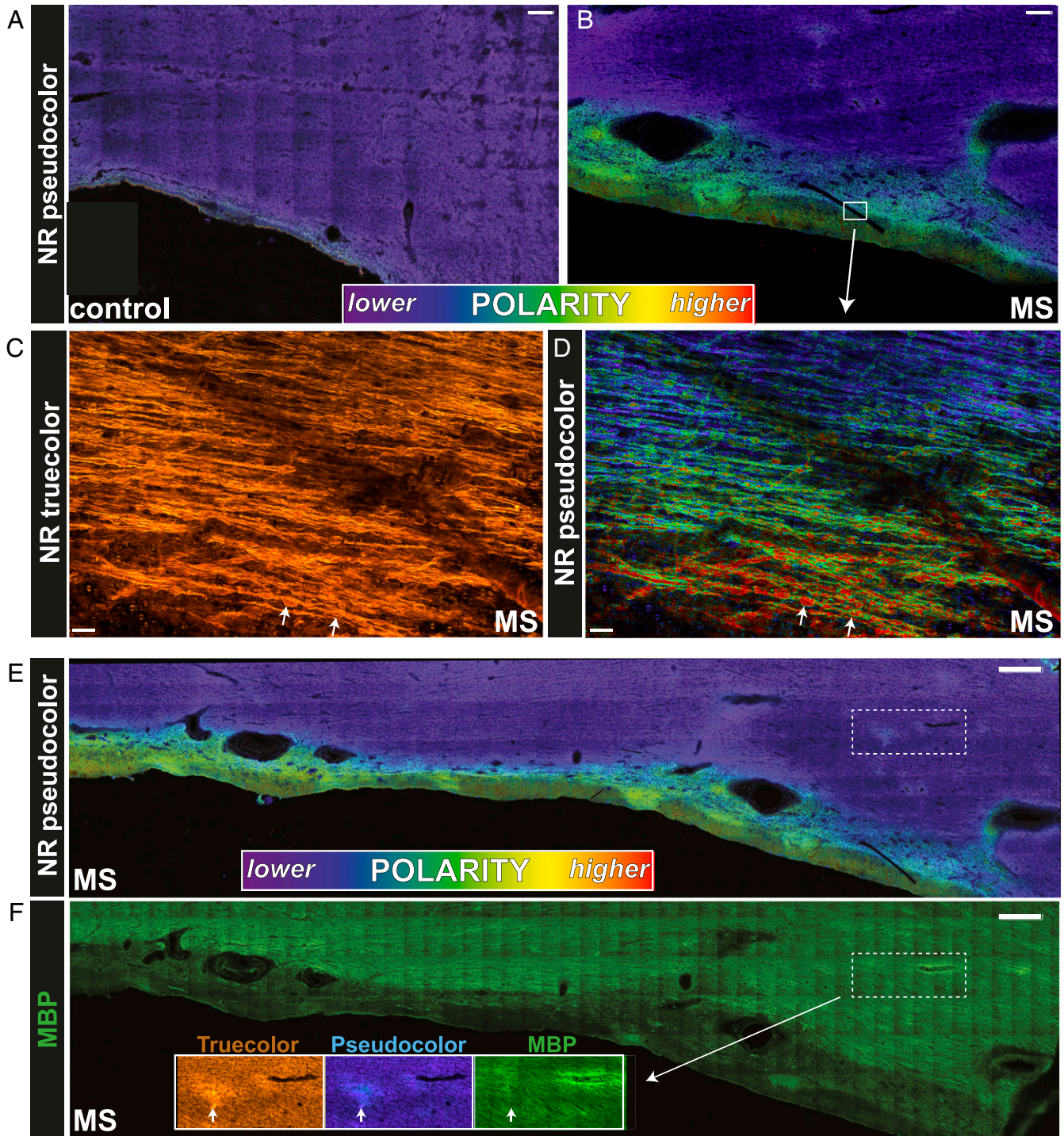
Fig. 4. Myelin in NAWM from human MS autopsied tissue exhibited significant spectroscopic changes. (*A*) NR fluorescence is relatively uniform in the periventricular region of a non-MS control with a nonpolar character. (*B*) By contrast, in MS tissue there was a gradient of spectral shift from the ventricular surface into the parenchyma. High-magnification true-color (*C*) and pseudocolor (*D*) images of the white box in *B* clearly depict this pathological gradient. White arrows in *C* and *D* point to swollen axons, increasing with proximity to the ventricle. Interestingly, the axonal spheroids exhibited a striking red appearance in the pseudocolor images, indicating a unique spectral signature and polar character that differed markedly from intact healthy fibers. (*E*) Periventricular MS tissue exhibited subtle focal abnormalities away from the ventricle (dotted white box), which were not seen in controls (*A*). (*F*) A closer analysis of the focal abnormality revealed by NR spectroscopy illustrates myelin that was intact by conventional immunohistochemsitry (MBP+, green) yet exhibited subtle change by NR spectroscopy. (Scale bars: *A* and *B*, 250 μm; *C* and *D*, 50 μm; *E* and *F*, 500 μm.)

Teo et al.
Nile Red fluorescence spectroscopy reports early physicochemical changes in myelin with
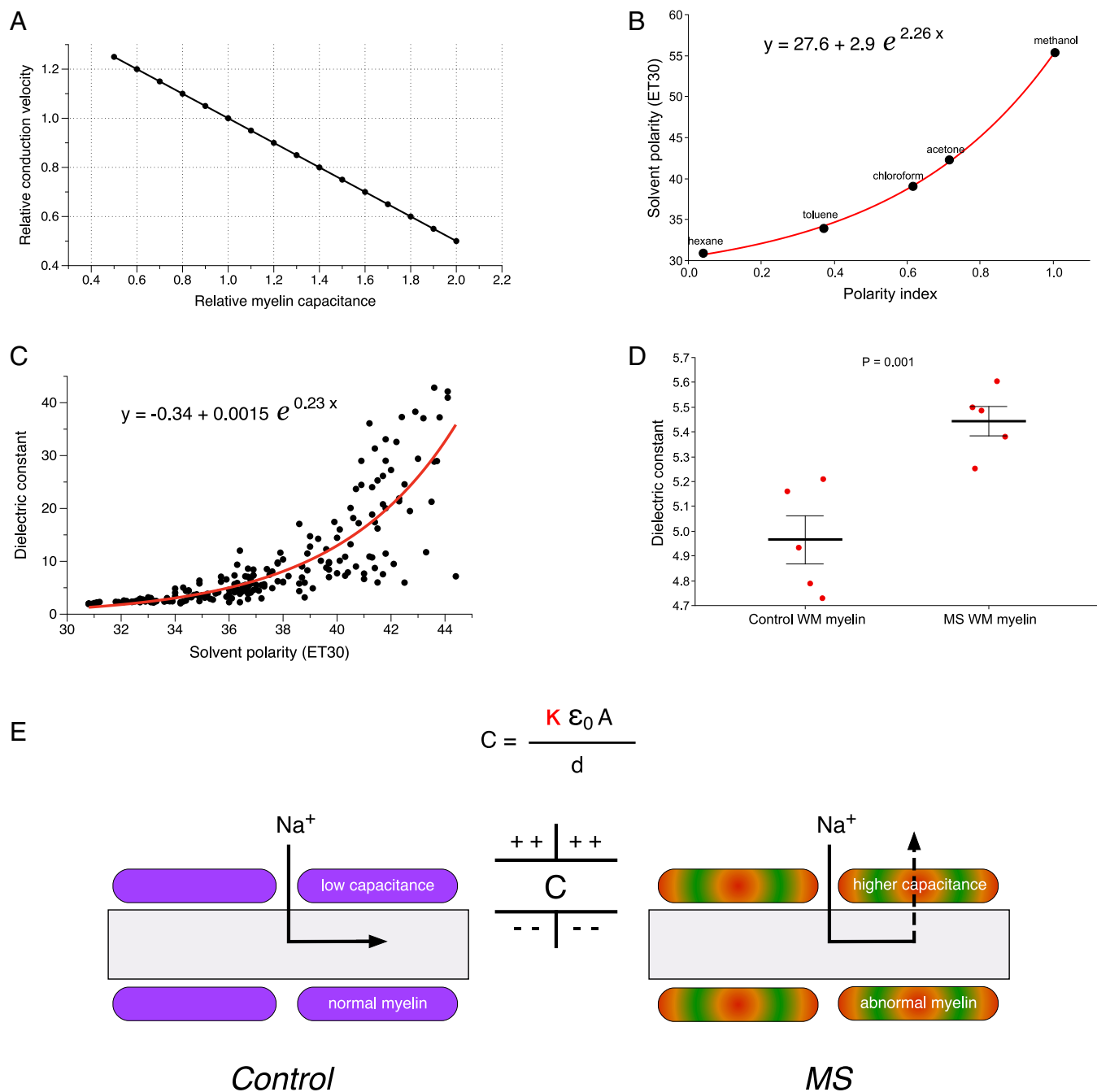high sensitivity

Fig. 5. Myelin in MS is diffusely abnormal in both normal-appearing white and gray matter. (*A*) True-color and pseudocolored images of MS NAWM stained with NR and analyzed in bulk (i.e., cells and extracellular matrix in a single region of interest). Pseudocolored images of MS tissue revealed a shift to longer wavelengths, indicating increased polarity compared to non-MS controls. (*B*) The graph depicting mean polarity index calculated from NR spectra. White matter exhibited a more polar character in MS, whereas gray matter shifted in the opposite direction. (*C*) MS NAWM myelin showed marked heterogeneity compared to control (arrows), with a corresponding shift to higher mean polarity (*D*). As with bulk tissue analysis, gray matter myelin had a lower polarity index in MS. The significance was determined by unpaired two-tailed *t* test. (Scale bars: *A*, 25 μm; *C*, 10 μm.) *$P < 0.05$.

of myelin in gray versus white matter (Fig. 2*C*), again with the former exhibiting a higher polarity. One explanation might involve different roles of myelin in gray and white matter. In the latter, axons may be chiefly responsible for efficient high-speed transmission and might therefore contain uniformly nonpolar sheaths (Fig. 5*D*) that would maximize conduction velocity (Fig. 6). In contrast, gray matter myelin might be more heterogeneous as it is deliberately modulated to adjust conduction and tune synchronization of neural networks (38). In support, in gray matter regions such as prefrontal cortex, areas that are not fully myelinated until adolescence, evidence indicates that morphological changes in myelin contribute to the acquisition of new motor skills such as

juggling and piano playing (39). In a mouse model, subtle changes in myelin internode length and number were recently identified as underpinning the formation of learning and memory (40). We propose that differences in polarity of myelin, stemming from differences in lipid chemical composition, lipid organization, and/ or hydration state of the myelin lamellae (41), might represent an additional means of modulating conduction velocity without the need for structural remodeling.

NR spectroscopy sensitively detected very early myelin pathology after treatment with CPZ, a toxin that causes delayed demyelination after oral ingestion. Only 2 d after beginning CPZ, we observed a significant spectral shift in otherwise intact myelinated

Teo et al.
Nile Red fluorescence spectroscopy reports early physicochemical changes in myelin with high sensitivity

PNAS | 7 of 11
https://doi.org/10.1073/pnas.2016897118

Fig. 6. Effects of altered myelin capacitance on axonal conduction velocity: theoretical calculations. (*A*) The graph of conduction velocity as a function of myelin capacitance. With all other geometrical properties held constant, propagation velocity is sensitive to myelin capacitance with an inversely linear relationship (48). (*B*) There is a close exponential relationship between polarity index calculated from NR spectra and published polarities for the five solvents used in our study. (*C*) Similarly, an exponential function was fitted to published dielectric constants versus solvent polarity for a variety of organic solvents (49). (*D*) Together, these calibration curves allowed us to estimate myelin dielectric constants using NR spectra acquired from myelin regions. Myelin from NAWM in MS brain had a significantly greater mean dielectric constant. The *P* value was calculated using unpaired one-tailed *t* test. (*E*) A model proposing how variations in myelin capacitance due to changes in dielectric constant alone (κ) could significantly alter action currents and therefore conduction velocities in still-myelinated axons with normal geometry (A and d: area and thickness of myelin + internodal axolemma, respectively; ε_0: permittivity of free space). Normal low-capacitance myelin will promote inward action currents to flow to the next node and excite it with minimal delay. In contrast, higher capacitance will cause more leakage of current across the internodal myelin, delaying activation of the next node or blocking conduction altogether.

axons of the corpus callosum, a region destined for eventual demyelination. The initial increased polarity likely results from an early loss of nonpolar lipids, which drain and accumulate in the periventricular regions; these were not enriched in cholesterol in the early stages (*SI Appendix*, Fig. S3). This could instead be due to

activation of enzymes such as plasmalogenase, leading to cleavage of nonpolar acyl chains from membrane lipids and depletion of these nonpolar species from the myelin (42, 43). This, in turn, would result in an excess of more polar lipids and proteins and/or a change in the lipid order of myelin membranes, resulting in more

hydrated bilayers and thus a more polar environment to which the NR molecules are exposed (41). Early tissue perturbations identified by NR spectroscopy mirror the metabolic responses and oligodendrocyte changes, including severe down-regulation of RNAs encoding myelin proteins (44), and evidence of dysregulation of iron homeostasis causing oligodendrocyte and myelin injury (45), resulting from even very brief CPZ exposure. This is consistent with early parallel changes in myelin lipids as reported by our spectroscopic method.

MS is characterized by fluctuating focal demyelinating lesions in both gray and white matter regions of the CNS (46, 47). Although traditionally considered to be due to multifocal attack by immune cells, detailed MRI and histological study suggests that the CNS is diffusely involved, resulting in subtle but widespread astro- and microgliosis, axonal damage, and minimal lymphocytic infiltration, but without overt myelin loss (29). As with early predemyelinating insults in the rodent, our method also detected substantial widespread abnormalities in autopsy samples of progressive MS brain outside of focal demyelinating lesions (so-called NAWM). Overall, bulk MS white matter exhibited significantly higher polarity compared to healthy age-matched controls (Fig. 5B), a spectroscopic shift similar to early changes following CPZ exposure in the rodent. Higher magnification images revealed even more striking differences at the level of the myelin sheaths. Still-myelinated axons were noted to have frequent spheroids (Fig. 5C, *SI Appendix*, Fig. S4), as is typical of NAWM (29). Intriguingly, the morphologically intact myelin was very spectroscopically heterogeneous (*SI Appendix*, Fig. S4, arrows) compared to controls and exhibited a significantly increased polarity (Fig. 5D). This could be due to preferential loss of less polar lipids and more disordered myelin lipid bilayers, as an early precursor to later breakdown of the myelin sheath.

Even in the absence of histological myelin thinning or loss, the physiochemical alteration of the sheath as reported by our method could have important functional consequences. Saltatory conduction along myelinated axons is strongly governed by resistive and capacitive properties, with velocity inversely proportional to myelin capacitance (48). Fig. 6 shows theoretical calculations of how changing myelin polarity with resulting change in dielectric constant could affect conduction velocity without overt changes in myelin geometry. In order to estimate changes in myelin capacitance, we converted the measured myelin polarity determined by NR fluorescence into dielectric constants using previously published parameters from organic solvents (49) (Fig. 6B). The exponential fits produced a calibration curve, which we used to compute dielectric constants of control and MS myelin. Based on our measurements, healthy CNS myelin had a mean dielectric constant of 8.2 ± 0.3 in gray matter and 5.0 ± 0.1 in white matter, which corresponds very well to previous estimates of ~5 to 10 (50). Notably, myelin from NAWM regions of MS brain exhibited a significantly higher mean dielectric constant (5.4 versus 5.0, $P = 0.001$). The predicted increase in MS myelin capacitance could translate into functionally significant impairment of conduction velocities throughout the MS brain (Fig. 6E). These estimates are based on overall averaged myelin dielectric constants; indeed, widespread multifocal regions of altered myelin capacitance as suggested by the subtle lesions in Fig. 4E could more profoundly exacerbate conduction abnormalities along the length of any particular axon. These changes could, in turn, explain the frequent and disabling nonfocal symptoms affecting MS patients such as fatigue, cognitive impairment, and depression (51) and are consistent with diffusion tensor imaging abnormalities in the white matter of cognitively impaired MS patients (52).

Moreover, given that subtle myelinopathy can elicit pathological autoimmune inflammation in the immune-predisposed host (53), our results provide additional support for the concept of how a primary myelin pathology, now possibly involving myelin lipids as a major component, could contribute to both ongoing degeneration and secondary autoimmune inflammation in MS. By helping elucidate subtle myelin lipid pathology, our method may guide a deeper understanding of MS pathophysiology and novel more effective therapeutic strategies.

Materials and Methods

Nile Red Solvent Mixtures for Generation of Reference Spectra. To obtain the fluorescence emission spectra of NR dissolved in various solvents, a small aliquot of dye dissolved at a concentration of 20 μM was drawn into glass capillary tubes (1 mm × 75 mm) via capillary action; then, both ends of the tube were sealed with Dow Corning vacuum grease. The NR-solvent mixtures were then excited by a 488-nm laser and spectral images acquired by an upright Nikon A1RMP spectral confocal microscope. Because of the poor quantum yield of NR in highly polar PBS, a higher concentration of NR (60 μM) was used to increase the signal to noise.

Lipid Depletion and Generation of Giant Unilamellar Vesicles. Approximately 200,000 MO3.13 cells (a human oligodendrocytic hybrid cell line) were plated on glass coverslips in 6-well plates. Cells were fixed with 4% paraformaldehyde for 1 h the following day, then washed once in PBS. For near-total nonspecific delipidation, the cells were transferred to glass wells to which chloroform:methanol (2:1 volume/volume) was added for overnight incubation at room temperature. Cells were rinsed in PBS and stained with NR along with nondelipidated controls (example of control cells with spectra from various subcellular regions is shown in *SI Appendix*, Fig. S5). Imaging was performed after a final quick rinse in PBS following NR staining. For selective depletion of cholesterol, cells were prepared as above, but instead of immersion in chloroform:methanol, 20 mM methyl-β-cyclodextrin (54) was added to fixed cells for overnight incubation at room temperature. Cells were then labeled with NR. Giant unilamellar vesicles (GUVs) were generated using an electroformation method adapted from Klymchenko et al. (55). DOPC and cholesterol were obtained from Avanti Polar Lipids. Briefly, a 0.1 mM solution of DOPC in chloroform was coated on indium tin oxide glass and transferred into a vacuum chamber for 1 h to be dried. The glass was then submerged in 300 mM sucrose, and a 2 to 3 V peak-peak 10 Hz alternating voltage was applied for 2 h at 42 °C. Then, a 2-mL aliquot of GUV solution was added to 8 mL of 300 mM glucose solution to yield a final product of GUVs for imaging. For cholesterol-doped GUVs, a 1:3 DOPC:cholesterol ratio was mixed in chloroform and GUVs prepared as above. Depletion of GUVs of cholesterol was done using 200 μM methyl-β-cyclodextrin overnight. For phospholipase experiments, 10 units of phospholipase A2 from honeybee venom (Sigma, CAS # 9001-84-7) was prepared in water and added directly to 1 mL final solution of GUVs and allowed to react for 40 min.

Animal Ethics. All animal experiments were carried out in accordance with protocols approved by the University of Calgary Animal Care Committee and guidelines from the Canadian Council on Animal Care.

Cuprizone Treatment. Male C57BL/6 mice (Charles River) aged 7 to 8 wk were fed standard mouse chow ad libitum containing 0.2% wt/wt CPZ for 2, 7, or 14 d.

Mouse Tissue Harvesting. Tissue was harvested for histopathology at appropriate times after CPZ. Under heavy sodium pentobarbital anesthesia, mice were transcardially perfused, first with 12 mL room temperature 1× PBS and then 12 mL ice-cold 4% paraformaldehyde. The tissue was postfixed in the same fixative at 4 °C overnight, after which it was cryoprotected first in 20% sucrose until the tissue sank and then 30% sucrose. Brains were embedded in optimal cutting temperature compound and rapidly frozen in dry ice–cooled isopentane. Depending on the experiment, sections were cut on a cryostat between 20 and 100 μm and collected on VWR Superfrost Plus Micro Slides (three sections per slide, region matched).

Nile Red Staining of Fixed Frozen Tissue Sections. A 6-mM stock solution of NR was prepared in DMSO and stored at −20 °C. The working concentration ranged from 10 to 25 μM in 1× PBS depending on the specimen size (20 μm versus 100 μm thickness). Fixed frozen tissue sections were stained with NR for 10 min, irrespective of section thickness, followed by a single 5-min rinse in PBS. The stained tissue sections were then submerged in PBS solution on a glass microscope slide and imaged with a water-immersion objective without mounting media or cover slipping.

Spectral Confocal Imaging and Image Processing. All images were collected following excitation with a 488 nm laser. Spectral fluorescence images were recorded using an upright Nikon A1RMP spectral confocal microscope with a

Teo et al.
Nile Red fluorescence spectroscopy reports early physicochemical changes in myelin with high sensitivity

PNAS | 9 of 11
https://doi.org/10.1073/pnas.2016897118

water immersion objective lens (25×, numerical aperture 1.1). Spectrometer resolution was 10 nm with 26 channels ranging between 490 nm and 740 nm. To standardize data analysis, all spectra were interpolated to 400 data points using cubic splines, and each spectrum was then normalized for comparison and spectral decomposition using ImageTrak image analysis software (http://stysneurolab.org/imagetrak/). For visualization of such multichannel spectral images, "true-color" renditions were calculated to approximate what the naked eye would see if looking at the samples directly. For spectral decomposition, two bracketing basis spectra were used to define the minimum and maximum polarity values represented by the most blue- and most red-shifted spectra, respectively. To generate pseudocolor images, a nonlinear transformation algorithm assigned a numerical index between 0 and 1 depending on the fit of a given pixel to the pair of bracketing reference spectra. This pixel was then assigned a pseudocolor ranging from violet (index 0) to red (index 1); nonpolar features in the image are therefore represented by cooler colors, while more polar elements appear in hotter colors. Such pseudocolor images provide greater sensitivity for discerning subtle spectral differences that the eye would not otherwise perceive when viewing true-color equivalents. Adjusting spectral brackets to expand a certain spectral subrange of interest allows excellent visualization of even very small spectral differences (*SI Appendix*, Fig. S5). The polarity index was defined as this numerical index produced by the nonlinear fitting. To select myelin for data analysis, rodent images were then randomly selected in the region of the corpus callosum, while images of human samples were masked by hand. Contaminating signal from laser backscatter was removed by a 490 nm long-pass filter.

Filipin III Staining for Cholesterol. Brain sections were stained using 1 μg/μL Filipin III (Cayman Chemical Company #70440) in PBS for 1 h, then washed twice with PBS for 5 min each.

Luxol Fast Blue Staining. Mouse sections were stained with Luxol fast blue (LFB) (Solvent Blue 38, Sigma-Aldrich) for myelin as previously described (53) and imaged using a Thorlabs EnVista whole-slide scanning microscope.

Immunohistochemistry. For repeat imaging of the same tissue section, NR was efficiently removed by processing tissue sections through a series of graded ethanol rinses (1 min each in water, 50, 70, 95, 100, 95, 70, and 50% ethanol, water), after which sections were blocked in 10% horse serum and 1% bovine serum albumin for 1 h at room temperature, then incubated with mouse anti-

MBP clone SMI99 (1:1,000; Biolegend #808401) overnight at 4 °C. The next day, the primary antibodies were rinsed in 1× PBS and the appropriate secondaries applied (1:500) for 1 h at room temperature.

Autopsy Information. MS human tissue was generously provided by the Netherlands Brain Bank at Vrije Universiteit University, Amsterdam (https://www.brainbank.nl/), including five individuals (age at death 66.2 ± 2.3) with progressive MS. The postmortem delay averaged 9 h (range: 6 to 18 h). Five age-matched (age at death 68.2 ± 3.0) control brain tissue samples were obtained from the Normal Aging Brain Collection Amsterdam (nabca.eu/), and the cause of death was not MS related. At autopsy, the collected brain regions were initially kept in 4% formalin, brain blocks were screened by MRI, and then transferred to PBS + 5% sucrose. After saturation, brain regions were stored at −30 °C. The brains of patients were then cut into coronal slices of 10 mm thickness. Based on MRI images of the coronal slice, regions mostly containing NAWM were isolated and mounted on slides. Slides were then stained by 20 μM NR in 1× PBS solution for 10 min and washed for 5 min once with PBS before spectral imaging.

Statistical Analysis. Statistical significance was calculated using R version 3.6.1 (56) using t test for comparison of two groups or ANOVA for comparison of multiple groups, followed by a post hoc Dunnett test, unless otherwise indicated. Every data point in each graph reflects a unique test subject, whether human or mouse.

Data Availability. Raw data are available upon request.

1. L. A. Horrocks, Composition of mouse brain myelin during development. *J. Neurochem.* **15**, 483–488 (1968).
2. N. Snaidero *et al.*, Antagonistic functions of MBP and CNP establish cytosolic channels in CNS myelin. *Cell Rep.* **18**, 314–323 (2017).
3. M. T. Weil *et al.*, Loss of myelin basic protein function triggers myelin breakdown in models of demyelinating diseases. *Cell Rep.* **16**, 314–322 (2016).
4. J. S. O'Brien, E. L. Sampson, Lipid composition of the normal human brain: Gray matter, white matter, and myelin. *J. Lipid Res.* **6**, 537–544 (1965).
5. M. L. Cuzner, A. N. Davison, The lipid composition of rat brain myelin and subcellular fractions during development. *Biochem. J.* **106**, 29–34 (1968).
6. M. J. Malone, M. C. Szoke, Neurochemical studies in aging brain. I. Structural changes in myelin lipids. *J. Gerontol.* **37**, 262–267 (1982).
7. W. T. Norton, S. E. Poduslo, Myelination in rat brain: Changes in myelin composition during brain maturation. *J. Neurochem.* **21**, 759–773 (1973).
8. S. G. Kohama, D. L. Rosene, L. S. Sherman, Age-related changes in human and non-human primate white matter: From myelination disturbances to cognitive decline. *Age (Dordr.)* **34**, 1093–1110 (2012).
9. B. Gerstl, M. J. Kahnke, J. K. Smith, M. G. Tavaststjerna, R. B. Hayman, Brain lipids in multiple sclerosis and other diseases. *Brain* **84**, 310–319 (1961).
10. C. Laule *et al.*, Diffusely abnormal white matter in multiple sclerosis: Further histologic studies provide evidence for a primary lipid abnormality with neurodegeneration. *J. Neuropathol. Exp. Neurol.* **72**, 42–52 (2013).
11. J. L. Kanter *et al.*, Lipid microarrays identify key mediators of autoimmune brain inflammation. *Nat. Med.* **12**, 138–143 (2006).
12. M. C. Ford *et al.*, Tuning of Ranvier node and internode properties in myelinated axons to adjust action potential timing. *Nat. Commun.* **6**, 8073 (2015).
13. S. Aggarwal *et al.*, Myelin membrane assembly is driven by a phase transition of myelin basic proteins into a cohesive protein meshwork. *PLoS Biol.* **11**, e1001577 (2013).
14. R. Shaharabani *et al.*, Structural transition in myelin membrane as initiator of multiple sclerosis. *J. Am. Chem. Soc.* **138**, 12159–12165 (2016).
15. S. Vikström, L. Li, A. Wieslander, The nonbilayer/bilayer lipid balance in membranes. Regulatory enzyme in Acholeplasma laidlawii is stimulated by metabolic phosphates, activator phospholipids, and double-stranded DNA. *J. Biol. Chem.* **275**, 9296–9302 (2000).
16. S. M. Gruner, Intrinsic curvature hypothesis for biomembrane lipid composition: A role for nonbilayer lipids. *Proc. Natl. Acad. Sci. U.S.A.* **82**, 3665–3669 (1985).
17. R. Shaharabani, M. Ram-On, Y. Talmon, R. Beck, Pathological transitions in myelin membranes driven by environmental and multiple sclerosis conditions. *Proc. Natl. Acad. Sci. U.S.A.* **115**, 11156–11161 (2018).
18. E. Muro, G. E. Atilla-Gokcumen, U. S. Eggert, Lipids in cell biology: How can we understand them better? *Mol. Biol. Cell* **25**, 1819–1823 (2014).
19. M. J. Cooper, M. W. Anders, High pressure liquid chromatography of fatty acids and lipids. *J. Chromatogr. Sci.* **13**, 407–411 (1975).
20. A. S. Mohammadi, N. T. N. Phan, J. S. Fletcher, A. G. Ewing, Intact lipid imaging of mouse brain samples: MALDI, nanoparticle-laser desorption ionization, and 40 keV argon cluster secondary ion mass spectrometry. *Anal. Bioanal. Chem.* **408**, 6857–6868 (2016).
21. A. R. Buchberger, K. DeLaney, J. Johnson, L. Li, Mass spectrometry imaging: A review of emerging advancements and future insights. *Anal. Chem.* **90**, 240–265 (2018).
22. K. W. C. Poon *et al.*, Lipid biochemical changes detected in normal appearing white matter of chronic multiple sclerosis by spectral coherent Raman imaging. *Chem. Sci. (Camb.)* **9**, 1586–1595 (2018).
23. P. Greenspan, S. D. Fowler, Spectrofluorometric studies of the lipid probe, nile red. *J. Lipid Res.* **26**, 781–789 (1985).
24. M. Romek, B. Gajda, E. Krzysztofowicz, M. Kepczynski, Z. Smorag, New technique to quantify the lipid composition of lipid droplets in porcine oocytes and pre-implantation embryos using Nile Red fluorescent probe. *Theriogenology* **75**, 42–54 (2011).
25. S. Nigam, S. Rutan, Principles and applications of solvatochromism. *Appl. Spectrosc.* **55**, 362A (2001).
26. H. P. Wacklin, F. Tiberg, G. Fragneto, R. K. Thomas, Distribution of reaction products in phospholipase A2 hydrolysis. *Biochim. Biophys. Acta* **1768**, 1036–1049 (2007).
27. S. K. Ludwin, Central nervous system demyelination and remyelination in the mouse: An ultrastructural study of cuprizone toxicity. *Lab. Invest.* **39**, 597–612 (1978).
28. L. Cantuti-Castelvetri *et al.*, Defective cholesterol clearance limits remyelination in the aged central nervous system. *Science* **359**, 684–688 (2018).
29. A. Kutzelnigg *et al.*, Cortical demyelination and diffuse white matter injury in multiple sclerosis. *Brain* **128**, 2705–2712 (2005).
30. J. Valanciunaite *et al.*, Polarity mapping of cells and embryos by improved fluorescent solvatochromic pyrene probe. *Anal. Chem.* **92**, 6512–6520 (2020).
31. D. M. Owen, C. Rentero, A. Magenau, A. Abu-Siniyeh, K. Gaus, Quantitative imaging of membrane lipid order in cells and organisms. *Nat. Protoc.* **7**, 24–35 (2011).
32. P. Greenspan, E. P. Mayer, S. D. Fowler, Nile red: A selective fluorescent stain for intracellular lipid droplets. *J. Cell Biol.* **100**, 965–973 (1985).

33. E. J. O'Rourke, A. A. Soukas, C. E. Carr, G. Ruvkun, C. elegans major fats are stored in vesicles distinct from lysosome-related organelles. *Cell Metab.* **10**, 430–435 (2009).

34. C. Reichardt, Solvatochromic dyes as solvent polarity indicators. *Chem. Rev.* **94**, 2319–2358 (1994).

35. H. Tajalli, A. Gilani, M. S. Zakerhamidi, P. Tajalli, The photophysical properties of Nile red and Nile blue in ordered anisotropic media. *Dyes Pigments* **78**, 15–24 (2008).

36. A. Ghanadzadeh Gilani, M. Moghadam, M. S. Zakerhamidi, Solvatochromism of Nile red in anisotropic media. *Dyes Pigments* **92**, 1052–1057 (2012).

37. E. Oldfield, D. Chapman, Molecular dynamics of cerebroside-cholesterol and sphingomyelin-cholesterol interactions: Implications for myelin membrane structure. *FEBS Lett.* **21**, 303–306 (1972).

38. S. Timmler, M. Simons, Grey matter myelination. *Glia* **67**, 2063–2070 (2019).

39. S. L. Bengtsson *et al.*, Extensive piano practicing has regionally specific effects on white matter development. *Nat. Neurosci.* **8**, 1148–1150 (2005).

40. C. L. Cullen *et al.*, Low-intensity transcranial magnetic stimulation promotes the survival and maturation of newborn oligodendrocytes in the adult mouse brain. *Glia* **67**, 1462–1477 (2019).

41. Y. Niko, P. Didier, Y. Mely, G. Konishi, A. S. Klymchenko, Bright and photostable push-pull pyrene dye visualizes lipid order variation between plasma and intracellular membranes. *Sci. Rep.* **6**, 18870 (2016).

42. E. M. Carey, N. M. Freeman, Biochemical changes in Cuprizone-induced spongiform encephalopathy. I. Changes in the activities of 2′,3′-cyclic nucleotide 3′-phosphohydrolase, oligodendroglial ceramide galactosyl transferase, and the hydrolysis of the alkenyl group of alkenyl, acyl-glycerophospholipids by plasmalogenase in different regions of the brain. *Neurochem. Res.* **8**, 1029–1044 (1983).

43. T. Yanagihara, J. N. Cumings, Alterations of phospholipids, particularly plasmalogens, in the demyelination of multiple sclerosis as compared with that of cerebral oedema. *Brain* **92**, 59–70 (1969).

44. J. Goldberg *et al.*, Short-term cuprizone feeding induces selective amino acid deprivation with concomitant activation of an integrated stress response in oligodendrocytes. *Cell. Mol. Neurobiol.* **33**, 1087–1098 (2013).

45. P. Jhelum *et al.*, Ferroptosis mediates cuprizone-induced loss of oligodendrocytes and demyelination. *J. Neurosci.* **40**, 9327–9341 (2020).

46. M. Calabrese *et al.*, Exploring the origins of grey matter damage in multiple sclerosis. *Nat. Rev. Neurosci.* **16**, 147–158 (2015).

47. T. Kuhlmann *et al.*, An updated histological classification system for multiple sclerosis lesions. *Acta Neuropathol.* **133**, 13–24 (2017).

48. J. W. Moore, R. W. Joyner, M. H. Brill, S. D. Waxman, M. Najar-Joa, Simulations of conduction in uniform myelinated fibers. Relative sensitivity to changes in nodal and internodal parameters. *Biophys. J.* **21**, 147–160 (1978).

49. J. P. Cerón-Carrasco *et al.*, Solvent polarity scales: Determination of new ET(30) values for 84 organic solvents. *J. Phys. Org. Chem.* **27**, 512–518 (2014).

50. T. Tsubo, M. Kurokawa, Verification of the effect of the axon fluid as a highly dielectric medium in the high-speed conduction of action potentials using a novel axon equivalent circuit. *Biophys. Physicobiol.* **15**, 214–228 (2018).

51. S. Abel *et al.*, Myelin damage in normal appearing white matter contributes to impaired cognitive processing speed in multiple sclerosis. *J. Neuroimaging* **30**, 205–211 (2020).

52. H. E. Hulst *et al.*, Cognitive impairment in MS: Impact of white matter integrity, gray matter volume, and lesions. *Neurology* **80**, 1025–1032 (2013).

53. A. V. Caprariello *et al.*, Biochemically altered myelin triggers autoimmune demyelination. *Proc. Natl. Acad. Sci. U.S.A.* **115**, 5528–5533 (2018).

54. S. Mahammad, I. Parmryd, Cholesterol depletion using methyl-β-cyclodextrin. *Methods Mol. Biol.* **1232**, 91–102 (2015).

55. A. S. Klymchenko *et al.*, Visualization of lipid domains in giant unilamellar vesicles using an environment-sensitive membrane probe based on 3-hydroxyflavone. *Biochim. Biophys. Acta* **1788**, 495–499 (2009).

56. R Core Team, *R: A Language and Environment for Statistical Computing* (R Foundation for Statistical Computing, Vienna, Austria, 2019).

NEUROSCIENCE